ChemComm

COMMUNICATION

View Article Online
View Journal | View Issue

Cite this: *Chem. Commun.*, 2023, 59, 720

Received 30th September 2022,
Accepted 12th December 2022

DOI: 10.1039/d2cc05369a

rsc.li/chemcomm

Solvent-tunable exciton-charge transfer mixed state enhances emission of functionalized benzo[*rst*]pentaphene through symmetry breaking†

Xiushang Xu,‡[a] Amy L. Vonder Haar,‡[b] Rengo Yoshioka,[a] Qizheng Zhang,[a] Serhii Vasylevskyi,[c] Andrew J. Musser*[b] and Akimitsu Narita*[a]

A benzo[*rst*]pentaphene (BPP) substituted by two bis(methoxyphenyl)amino (MeOPA) groups (BPP–MeOPA) was synthesized and clearly characterized by NMR and single-crystal X-ray analysis. Detailed investigations of its photophysical properties, including transient absorption spectroscopy analyses, revealed that the introduction of the MeOPA groups breaks the symmetry of the BPP core, improving its absorption and emission from an S_1 state with both excitonic and charge-transfer character.

Polycyclic aromatic hydrocarbons (PAHs) are a promising building block for functional materials in photonics, optoelectronics, and spintronics due to their intriguing optoelectronic and magnetic properties.[1–4] Many experimental and theoretical studies have demonstrated that these properties strongly depend on their size, shapes, and edge structures, such as armchair and zigzag.[5,6] PAH optoelectronic properties can be further modified by core functionalization, typically with electron-donating or -withdrawing groups.[7–10]

Benzo[*rst*]pentaphene (BPP), initially reported by Scholl and Neumann in 1922,[11] features a combination of zigzag and armchair edges, and can be a promising candidate for studying the effects of structural modification on the physicochemical properties toward different photonic applications. Nevertheless, despite the development of simplified synthetic methods for BPP,[12–16] its covalent functionalization with electron-donating/-withdrawing groups has been scarcely investigated. Recently, we reported that the relatively low photoluminescence quantum yield (PLQY, 13%) of BPP was due to its symmetry-forbidden electronic transitions.[17] Interestingly, a dimer of BPP, 5,5′-bibenzo[*rst*]pentaphene (BBPP) displayed symmetry-breaking charge transfer between two BPP units and enhanced PLQY (44%). However, BBPP was still dominated by the same underlying electronic structure characterized by a low-lying dark state; the enhancement in PLQY arose principally from a reduction of the energy gap between bright and dark states, resulting in more efficient intensity borrowing.

In this work, we synthesized 2,11-di-*tert*-butyl-N^5,N^5,N^8,N^8-tetrakis(4-methoxyphenyl)benzo[*rst*]pentaphene-5,8-diamine (BPP–MeOPA **1**), functionalizing the BPP core with two bis(4-methoxyphenyl)amino (MeOPA) groups that have been widely used for preparing organic hole-transporting materials due to their strong electron-donating ability.[18,19] The photophysical properties of BPP–MeOPA **1** were investigated using transient absorption and photoluminescence spectroscopies in comparison with the parent BPP **7**, revealing solvent polarity-dependent intramolecular charge transfer and enhanced PLQY.

For the synthesis of **1** and **7**, 2-bromo-4-(*tert*-butyl)-1-iodobenzene (**3**) was initially prepared from the commercially available 2-bromo-4-(*tert*-butyl)aniline (**2**) by Sandmeyer reaction in 98% yield (Scheme 1). Then, **3** was subjected to the regioselective halogen–metal exchange reaction with isopropylmagnesium chloride at −78 °C, and reacted with dimethylformamide (DMF) to afford aldehyde **4** in 77% yield. Subsequently, dialdehyde **6** was obtained by Suzuki–Miyaura coupling of **4** and diboronic ester **5** in 85% yield. Di-*tert*-butyl-substituted BPP **7** was prepared by dehydrative π-extension (DPEX) reaction of **5**.[15] Next, **7** was brominated by *N*-bromosuccinimide (NBS) to give dibromo-BPP **8** in 94% yield. Finally, BPP–MeOPA **1** was obtained by Buchwald–Hartwig coupling of **8** and di-4-methoxyphenylamino (MeOPA) in 87% yield. The chemical structure of BPP–MeOPA **1** was unambiguously characterized by mass spectrometry, nuclear magnetic resonance (NMR), and X-ray crystallography. Moreover, all proton NMR signals could be clearly assigned by

[a] *Organic and Carbon Nanomaterials Unit, Okinawa Institute of Science and Technology Graduate University, 1919-1 Tancha, Onna-son, Kunigami-gun, Okinawa 904-0495, Japan. E-mail: akimitsu.narita@oist.jp*
[b] *Department of Chemistry & Chemical Biology, Cornell University, Ithaca, NY 14850, USA. E-mail: ajm557@cornell.edu*
[c] *Engineering Section, Research Support Division, Okinawa Institute of Science and Technology Graduate University, 1919-1 Tancha, Onna-son, Kunigami-gun, Okinawa 904-0495, Japan*

† Electronic supplementary information (ESI) available. CCDC 2194433. For ESI and crystallographic data in CIF or other electronic format see DOI: https://doi.org/10.1039/d2cc05369a

‡ These authors contributed equally to this work.

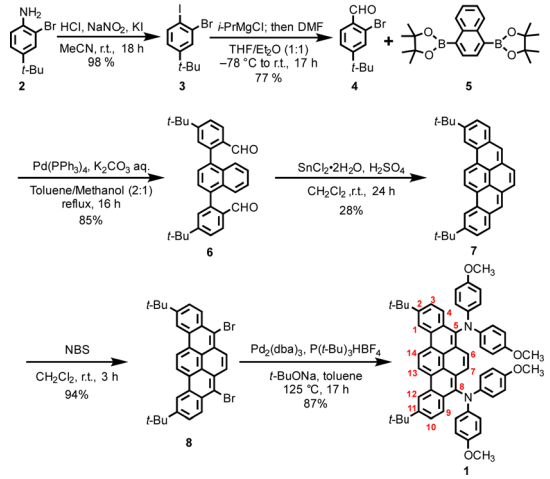

Scheme 1 The synthetic route to BPP–MeOPA **1** and BPP **7**.

^{1}H–^{1}H correlation spectroscopy (COSY) and nuclear Overhauser enhancement spectroscopy (NOESY) techniques (Fig. S11, S13 and S14, see ESI† for further details).

The single crystal of BPP–MeOPA **1** was successfully grown from evaporation of CH_2Cl_2/CH_3OH solution, enabling its structural determination by single-crystal X-ray analysis (Fig. 1). The single-crystal structure of **1** clearly revealed the BPP core and MeOPA substitutes at positions of C5 and C8 of BPP. The MeOPA was almost perpendicular to the BPP plane (dihedral angles 79°). In the crystal, along the *a*-axis, two BPP–MeOPA **1** are stacked almost parallel to each other. The plane-to-plane distance is 7.21 Å, indicating an absence of interactions between BPP–MeOPA **1** due to the existence of the *tert*-butyl and MeOPA groups at the peripheral position. Additionally, the X-ray structure is in good agreement with the one optimized by density functional theory (DFT) calculations.

The UV-vis absorption spectra of **1** and **7** were measured in toluene solutions (Fig. 2a). **1** and **7** display similar absorption peaks except for the low-energy absorption bands. The small peak located at 425 nm was observed for **7**, indicating the presence of the dark, symmetry-forbidden singlet state S_1, in agreement with our previous results.[17] The steady-state absorption of **1** suggests a comparable underlying electronic structure, but with noteworthy modifications. Most evidently, **1** displays a redshifted and broader low-energy absorption peak (502 nm) than that of **7**. The bathochromic shift of **1** reveals a reduced S_1

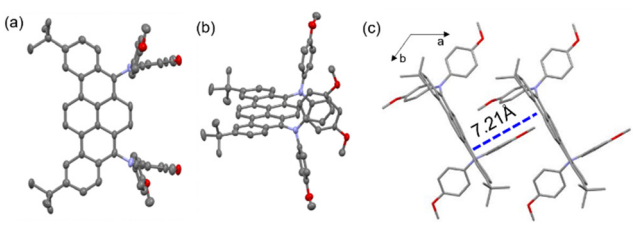

Fig. 1 Single-crystal structure of **1**, (a) top view, (b) side view (thermal ellipsoids shown at 50% probability); (c) Packing arrangement of **1** in the crystal (solvents are omitted for clarity).

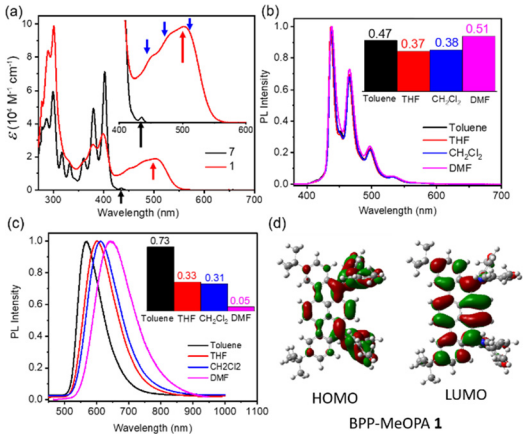

Fig. 2 (a) Molar absorptivity of compounds **1** and **7** measured in toluene. Inset: The forbidden S_1 absorption peaks of **1** and **7** is indicated by arrows, approximate locations of vibronic structure marked with blue arrows. Normalized PL spectra of **7** (b) and **1** (c) were measured in toluene, tetrahydrofuran (THF), dichloromethane (CH_2Cl_2), and DMF. The absolute PL quantum yields (PLQY) in toluene, THF, CH_2Cl_2, and DMF are shown in the legend. (d) HOMO/LUMO distributions for BPP–MeOPA **1** were calculated using density functional theory (DFT) on the B3LYP/6-311G(d,p) energy level.

energy gap, which can be ascribed to the electron-donating property of the MeOPA groups and the delocalization of frontier orbitals. The absorption of the principal BPP bright state is unaffected, and we observe the same vibronic progression from 350–400 nm as in **7**. The lowest-energy band exhibits strikingly enhanced molar extinction coefficient in **1** ($\varepsilon \sim 19\,000\ M^{-1}\ cm^{-1}$) compared to the S_1 state in **7** ($\varepsilon \sim 1200\ M^{-1}\ cm^{-1}$), and at the same time there is clear reduction in the absorption of the S_2 state ($\varepsilon \sim 70\,000\ M^{-1}\ cm^{-1}$ in **7** *versus* $\varepsilon \sim 32\,000\ M^{-1}\ cm^{-1}$ in **1**). While some of the latter effect arises from increased broadening in **1**, integration across the band confirms a dimming of the S_2 transition. These effects are consistent with enhanced S_1 intensity borrowing[17] from S_2. We propose that part of this enhancement in **1** relative to **7** arises from symmetry breaking. The BPP core and MeOPA moieties interact electronically through charge-transfer coupling, discussed further below, resulting in significant contributions to the wavefunction out of the BPP plane. This coupling is sensitive to the dihedral conformations around the amines. Such angles correspond to several low-frequency vibrational modes, resulting in significant geometric fluctuations and accordingly a reduction in the symmetry. This effect yields increased electronic disorder relative to **7**, broadening the vibronic progression observed in S_1 and S_2 and brightening the S_1 transition.

To gain further insight into the photophysical properties of **1** and **7**, their emission spectra were measured (Fig. 2b and c). Both molecules exhibit mirror-image emission from their S_1 states with minimal Stokes shift, and the emission maximum in toluene red-shifted from 437 nm in **7** to 569 nm in **1**. Whereas **7** exhibits well-defined vibronic structure including $0 \rightarrow 0$, $0 \rightarrow 1$, $0 \rightarrow 2$ and $0 \rightarrow 3$ transitions, the PL of **1** is broad and featureless. The disappearance of well-defined vibronic structure suggests a modified emission mechanism characteristic of intramolecular

charge-transfer (ICT) states.[21] Indeed, **1** uniquely displays a considerable emission redshift and decrease in PLQY with increasing solvent polarity, a signature of ICT emission (Fig. 2b and c). The formation of an ICT state in **1** upon photoexcitation is consistent with DFT calculations. The highest occupied molecular orbital (HOMO) is principally localized on the MeOPA units, while the lowest unoccupied molecular orbital (LUMO) is located on the BPP core (Fig. 2d). Time-dependent DFT calculations at M06-2X/6-311G(d,p) level indicate the lowest energy state contains major contributions from CT excitations, indicating partial electron transfer from MeOPA to BPP units (Fig. S16 and Table S1, ESI†). Intriguingly, this effect appears to significantly enhance the luminescence of the molecule. The absolute PLQY of **1** in toluene was estimated to be 0.73, much higher than that of **7** (0.47). In principle, spatial separation of electron and hole wavefunctions results in reduction of the absorptivity and emissivity of a state (Fig. S16, ESI†), so the enhancement of these quantities in **1** is surprising.

We used transient absorption (TA) spectroscopy to understand this behaviour. TA is a time-resolved technique for measuring fast, dynamic state evolutions induced in a molecule by photoexcitation. A pump pulse resonantly promotes electrons into higher energy excited states. A subsequent probe pulse interrogates the formation, transformation, and decay of states generated by the pump at a range of delay times after excitation. Presented as the normalized change of probe transmittance $\Delta T/T$, the resulting TA spectra combine three primary features: the ground state bleach ($\Delta T/T > 0$), which monitors the total population of molecules removed from the ground electronic state; the stimulated emission ($\Delta T/T > 0$), which results from photon emission by electrons returning to ground state when triggered by the probe; and the photoinduced absorption ($\Delta T/T < 0$), which reflects absorption of excited states to still higher levels. State lifetimes determined *via* TA can also be used to characterize non-radiative decay. We performed TA on BPP–MeOPA **1** in five solvents that span a range of polarities: DMF, pyridine (Py), THF, chlorobenzene (CB), and toluene (Tol) at a concentration of ~20 μg mL^{-1} (Fig. 3a and Fig. S19, ESI†). We present data for resonant S_1 excitation at 490 nm. Within our temporal resolution (200 fs), we observe no change in the excited-state decay pathway following excitation at 400 nm directly into the S_2 state, with only slight spectral broadening due to excess thermal energy (Fig. S20, ESI†).

All spectra show ground-state bleaching as a positive feature near 500–525 nm, in agreement with the red edge of the steady state absorption. Stimulated emission features are not distinguishable, likely indicating that the radiative transition does not have high brightness and is overpowered by the overlapping photoinduced absorption, the primary feature observed and spanning 525–825 nm. The initial state in the photoinduced absorption in all solvents exhibits fine structure with peaks ~660 nm, 710 nm, and 750 nm. On longer timescales we resolve a different spectral signature, with partial (toluene) or complete (all others) loss of this structure and the appearance of two distinct peaks. These then decay uniformly on an approximately nanosecond timescale. This stark change in spectral

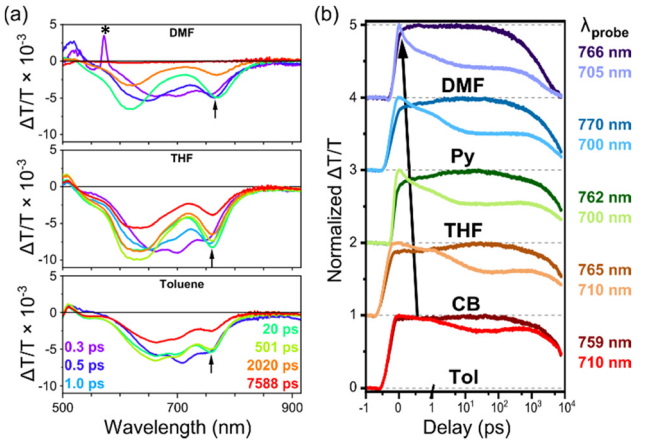

Fig. 3 (a) TA spectra of **1** with 490 nm excitation in DMF, THF, and toluene. * denotes coherent artifact. Arrows highlight the position of the CT-related band shared by both states. (b) TA kinetic traces, including for pyridine and chlorobenzene, chosen to highlight the dynamics for the initial state (shorter λ) and final state (longer λ). Traces are offset for clarity. The arrow is to guide the eye along solvent dependence of crossover point.

shape indicates a change in electronic state and reveals that two excited states are required to explain the properties of **1**. Importantly, we observe systematic differences in this general pathway as a function of solvent polarity (Fig. 3b). The final two-peak structure is most evident in highly polar DMF, while in toluene the spectral evolution is only partial, and we observe signs of the initial three-peaked structure throughout the measurement range. Moreover, the rate of this conversion tracks with solvent polarity: the initial state is barely resolved in DMF and evolves within 500 fs, while the corresponding spectral evolution in toluene requires over 10 ps. Similarly, the lifetime of the terminal state, which ranges from 2 ns in DMF to ~16 ns in toluene (Fig. S28 and Table S7, ESI†).

We can identify the final state observed in TA through comparison with time-resolved photoluminescence (PL) spectroscopy experiments. We observe the same positive solvatochromism reported in Fig. 2c, with no change in emission spectral shape during the measurement duration nor with change in excitation wavelength (Fig. S23, ESI†). As this ICT-like emission is stabilized with increasing solvent polarity, we see that the emission lifetime simultaneously decreases (Fig. 4a). The lifetimes range from

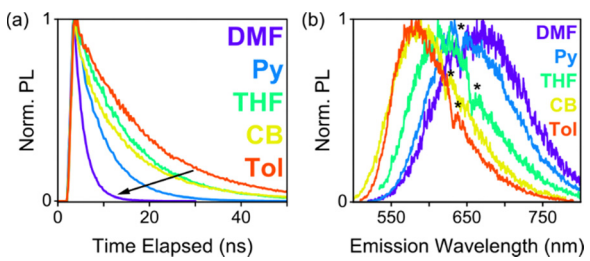

Fig. 4 (a) Solvent-dependent integrated PL dynamics of **1** following 490 nm excitation, and (b) corresponding normalized emission spectra. A systematic red shift and decrease in emission lifetime is observed with increasing polarity. * denotes a detector artifact.

approximately 2 ns in DMF to 11 ns in THF to ~16 ns in toluene. As lifetime decreases, the PL quantum yield drops precipitously, becoming only 5% in DMF relative to 73% in toluene (Fig. 2), suggesting a significant increase in nonradiative decay rate with stabilization. The slow PL decay dynamics closely follow the slow kinetics of the terminal state observed in TA (Fig. S26 and S28, ESI†), and we can thus assign the long-lived, two-peaked signature to a solvent-stabilized ICT state.[21] Electrochemical reduction of **1** to generate the signature of BPP radical anions (Fig. S24, ESI†) confirmed the presence of BPP anionic character in the primary TA bands and thus an ICT state.[21]

This assignment suggests that the initial photoexcited state, S_1, is not itself an ICT state, as it exhibits different excited-state lineshape. Indeed, the vibronic structure in the $S_0 \rightarrow S_1$ steady-state absorption (Fig. S29, ESI†) is typically characteristic of excitonic, rather than CT, species.[20,21] However, we note that the initial and ICT states share a common photoinduced absorption peak at approximately 750 nm (arrows in Fig. 3a). Furthermore, the 615 nm ICT state peak forms *via* a progressive blue shift from a 650 nm shoulder present in the initial state. Given this state is optically allowed with vibronic structure, shares spectral features with ICT, and can be induced to form an ICT state through solvent interactions, we propose that the initial S_1 state is a mixed state.[20,21] It has both excitonic and CT character, which can relax into a weakly emitting, stabilized, pure ICT state through solvent dipole interactions.[20,21] In toluene, the solvent stabilization is relatively minor, resulting in only the slight enhancement of the CT character and favouring the bright mixed S_1 state.

This model highlights the delicate balance of factors governing the photophysics of **1**. Functionalization with MeOPA groups dynamically breaks the symmetry of this BPP derivative, allowing the S_1 state to become significantly brighter in absorption and emission. However, this effect comes at a cost: greatly increased susceptibility to form a stabilized ICT state with minimal orbital overlap and rapid nonradiative decay. Only in non-polar toluene are these competing factors balanced, to harness the advantages of symmetry-breaking functionalization without relaxation from the mixed S_1 state.

In summary, we have demonstrated the synthesis of donor–acceptor molecule BPP–MeOPA which was proved by X-ray crystallography. Photophysical properties of BPP–MeOPA were studied, which demonstrated intramolecular CT interactions and enhanced emission compared to BPP. Femtosecond TA spectroscopy in solutions of different polarity revealed that the S_1 state of BPP–MeOPA is mixed with both excitonic and CT character, which resulted in significantly brighter absorption and emission. This work demonstrates that there is great scope to enhance the optoelectronic properties of BPP chromophores and paves the way towards the development novel types of charge transfer in PAH derivatives to tune their optoelectronic properties and overcome their symmetry restrictions.

We acknowledge the financial support from the Okinawa Institute of Science and Technology Graduate University (OIST), JSPS KAKENHI Grant No. JP19K24686, and the Cornell Center for Materials Research (NSF DMR-1719875). Acknowledgment is made to the donors of The American Chemical Society Petroleum Research Fund for partial support of this research. We also appreciate the help and support provided by the Instrumental Analysis Section and the Scientific Computing and Data Analysis Section of Research Support Division at OIST. AVH gratefully acknowledges A. Halder, J. Ling, Y. Lai, and D. Bain for assistance with reference experiments.

Conflicts of interest

There are no conflicts to declare.

Notes and references

1 A. Narita, X. Y. Wang, X. L. Feng and K. Müllen, *Chem. Soc. Rev.*, 2015, **44**, 6616–6643.
2 X. S. Xu, K. Müllen and A. Narita, *Bull. Chem. Soc. Jpn.*, 2020, **93**, 490–506.
3 I. R. Márquez, S. Castro-Fernández, A. Millán and A. G. Campaña, *Chem. Commun.*, 2018, **54**, 6705–6718.
4 W. Chen, F. Yu, Q. Xu, G. Zhou and Q. Zhang, *Adv. Sci.*, 2020, **7**, 1903766.
5 Z. Y. Liu, S. Fu, X. M. Liu, A. Narita, P. Samori, M. Bonn and H. I. Wang, *Adv. Sci.*, 2022, **9**, 2106055.
6 X.-Y. Wang, X. Yao and K. Müllen, *Sci. China: Chem.*, 2019, **62**, 1099–1144.
7 A. Keerthi, I. C.-Y. Hou, T. Marszalek, W. Pisula, M. Baumgarten and A. Narita, *Chem. – Asian J.*, 2016, **11**, 2710–2714.
8 Y. Hu, L. F. Dössel, X.-Y. Wang, S. Mahesh, W. Pisula, S. De Feyter, X. Feng, K. Müllen and A. Narita, *ChemPlusChem*, 2017, **82**, 1030–1033.
9 Q. Chen, D. Wang, M. Baumgarten, D. Schollmeyer, K. Müllen and A. Narita, *Chem. – Asian J.*, 2019, **14**, 1703–1707.
10 Y.-Z. Tan, B. Yang, K. Parvez, A. Narita, S. Osella, D. Beljonne, X. Feng and K. Müllen, *Nat. Commun.*, 2013, **4**, 2646.
11 H. N. R. Scholl, *Chem. Ber.*, 1922, **55**, 118–126.
12 E. Clar, *Ber. Dtsch. Chem. Ges.*, 1939, **72**, 1645–1649.
13 R. G. Harvey, J. Pataki, C. Cortez, P. Di Raddo and C. X. Yang, *J. Org. Chem.*, 1991, **56**, 1210–1217.
14 F.-J. Zhang, C. Cortez and R. G. Harvey, *J. Org. Chem.*, 2000, **65**, 3952–3960.
15 D. Lungerich, O. Papaianina, M. Feofanov, J. Liu, M. Devarajulu, S. I. Troyanov, S. Maier and K. Amsharov, *Nat. Commun.*, 2018, **9**, 4756.
16 X. Xu, A. Kinikar, M. D. Giovannantonio, P. Ruffieux, K. Müllen, R. Fasel and A. Narita, *Bull. Chem. Soc. Jpn.*, 2021, **94**, 997–999.
17 X. Xu, S. Gunasekaran, S. Renken, L. Ripani, D. Schollmeyer, W. Kim, M. Marcaccio, A. Musser and A. Narita, *Adv. Sci.*, 2022, **9**, 2200004.
18 P. Murugan, T. Hu, X. Hu and Y. Chen, *J. Mater. Chem. A*, 2022, **10**, 5044–5081.
19 S. Shahnawaz, S. Sudheendran Swayamprabha, M. R. Nagar, R. A. K. Yadav, S. Gull, D. K. Dubey and J.-H. Jou, *J. Mater. Chem. C*, 2019, **7**, 7144–7158.
20 W. Li, Y. Pan, R. Xiao, Q. Peng, S. Zhang, D. Ma, F. Li, F. Shen, Y. Wang, B. Yang and Y. Ma, *Adv. Funct. Mater.*, 2014, **24**, 1609–1614.
21 A. M. Alvertis, S. Lukman, T. J. H. Hele, E. G. Fuemmeler, J. Feng, J. Wu, N. C. Greenham, A. W. Chin and A. J. Musser, *J. Am. Chem. Soc.*, 2019, **141**, 17558–17570.